2016

# DTI-Based Connectivity in Isolated Neural Ganglia: A Default Structural Graph in a Small World Framework

Abdol Aziz O. Ould Ismail

FLORIDA STATE UNIVERSITY

COLLEGE OF ENGINEERING

# DTI-BASED CONNECTIVITY IN ISOLATED NEURAL GANGLIA:

# A DEFAULT STRUCTURAL GRAPH IN A SMALL WORLD FRAMEWORK

By

ABDOL AZIZ O. OULD ISMAIL

A Thesis submitted to the
Department of Chemical and Biomedical Engineering
in partial fulfillment of the
requirements for the degree of
Master of Science

2016

Abdol Aziz Ould Ismail defended this thesis on February 17, 2016.
The members of the supervisory committee were:

Samuel C. Grant
Professor Directing Thesis

Jingjiao Guan
Committee Member

Yan Li
Committee Member

The Graduate School has verified and approved the above-named committee members, and certifies that the dissertation has been approved in accordance with university requirements.

*This thesis is dedicated to my three favorite families in the world: My family (especially Mama and Baba), the Elmoustaphas (especially Maymouna), and the Wagners (especially Leslie).*

# ACKNOWLEDGMENTS

First of all, I would like to acknowledge my supervisor Dr. Grant for the great teacher, researcher, and mentor he is. I must thank him for guiding me through experimental design and data acquisition and analysis, helping me patiently to develop myself in a field in which I had little background, and pushing me to be a better engineer and scientist. Because of him, I developed the great passion I have for MR techniques, and I built solid confidence that I can always learn and produce with hard work and determination. Sam, I am very fortunate to be your student. I also must acknowledge both the FAMU-FSU College of Engineering and the National High Magnetic Field Laboratory for providing me with the necessary techniques and financial support that were needed to complete this project. I would also like to thank Dr. Jens Rosenberg for his technical help in both acquiring and analyzing data. Every time I faced a technical problem or needed an answer, I did not hesitate to knock on his office door and he was always happy to help. Additionally, it is important to note that this work could not have been done in this specific fashion without Dr. Richard Bertram. I consider myself lucky to have found out about his great course this past fall. He introduced me to graph theory for the first time, and helped me over and over with his feedback on the graph theoretical analysis performed in this thesis. Thank you Dr. Bertram. In addition, I must acknowledge my committee members starting with Dr. Grant and his countless edits and corrections of my drafts and Dr. Li and Dr. Guan for their immediate response agreeing to be a part of the assessment of my thesis. It is an honor to be evaluated by you and I truly appreciate your time and guidance. Last but not least, I must acknowledge the student members of Dr. Grant's laboratory: Nastaren, Ghoncheh, David, Lee, Uriel, and Scott. Thanks guys for being there for me whenever I need help with my work, or just need to talk or eat or have a cup of tea or coffee with a friend.

# TABLE OF CONTENTS

# LIST OF TABLES

# LIST OF FIGURES

# ABSTRACT

Diffusion Tensor Imaging (DTI) provides a unique contrast based on the restricted directionality of water movement in an anisotropic environment. As such, DTI-based tractography can be used to characterize and quantify the structural connectivity within neural tissue. Here, DTI-based connectivity within isolated abdominal ganglia (ABG) of *aplysia Californica* is analyzed using network theory. In addition to quantifying the regional physical proprieties of the fractional anisotropy (FA) and apparent diffusion coefficient (ADC), DTI tractography was used to probe inner-connections of local communities, yielding unweighted, undirected graphs that represent community structures. Local and global efficiency, characteristic path lengths and clustering analysis are performed on both experimental and simulated data. The relevant intensity and velocity by which these specific nodes communicate is probed through weighted clustering coefficient measurements for the descriptive weighted matrices. Both small-worldness and novel small world metrics were used as tools to verify the small-world properties for the experimental results. The aim of this manuscript is to categorize and quantify the properties exhibited by structural networks in a model neural tissue to derive unique mean field information that quantitatively describe macroscopic connectivity. For ABG, findings demonstrate a default structural network with preferential specific small-world properties when compared to simulated lattice and random networks that are equivalent in order and degree.

**Keywords:** Diffusion Tensor Imaging, Structural Connectivity, Graph theory, Small World Networks, Binary and Weighted Graphs, Clustering Coefficient, Graph Efficiency, Characteristic Path Length, Lattice and Random Graphs, Watts-Strogatz Model, Small-worldness, Novel Small-world metric, Fractional Anisotropy.

# CHAPTER 1

# SIGNIFICANCE

Diffusion Tensor Imaging (DTI) based tractography continues to be a prime approach for reconstructing structural neuronal connectivity in a non-invasive and non-destructive fashion, yet quantitative assessments of the networks that correspond to these inner-connections are still limited and somewhat variable in the definition of standardized network parameters. This study is the first to demonstrate a default structural connectivity non-destructively in a small world framework for isolated neural ganglia with impressively consistent network properties. The mathematical characteristics of the nodes in neural graphs are potential biomarkers that may play a critical role in diagnosis and monitoring if applicable to clinical data. The findings of this work present significant advancement in applying graph theory to biomedical imaging of neural topology.

# CHAPTER 2

# INTRODUCTION

With increasing interest in neural networks and brain organization, the investigation of mathematical properties through either group or graph representatives to assess the connectivity between regions of interest continues to be a focal area in the study of neural topology. The simplicity of the one-dimensional analysis in graph theory is the driving force behind its popularity among ecologists. Although a group theory application would take a multi-dimension approach with consideration for the descriptive geometry of the exhibited paths that connect graph components, many applications that model real networks rely on graph theory. Applications of graph theory are growing and diverse, including various areas such as urban planning (Roberts 1978 ), landscape connectivity (Urban and Keitt 2001 ), social networks (Newman, et al. 2002 ), and structural (de Reus, et al. 2014 ) and functional connectivity (He and Evans 2010 ) in complex biological networks (Bullmore and Sporns 2009 ). In graph approaches, system variables are reduced to cut computational cost and maintain the uniqueness of provided solutions. In addition to the lack of spatial description of the connecting curves, these connections are considered instantaneous. As a result, many of the derived graph properties reveal more about the centrality and clustering of the individual end points at the cost of the spatial and symmetrical feedback of the connections.

The network of interest in this study is the structural connectivity in the abdominal ganglion (ABG) of *aplysia Californica*, which is a recognized model for neural tissue including synaptic transmission (Klein and Kandel 1978 ), cellular learning and memory (Frost and Kandel 1995 ), behavioral conditioning (Jing, et al. 2004 ; Vorster, et al. 2014 ), proteomics (Birner-Gruenberger, et al. 2012 ), aging (Akhmedov, et al. 2013 ), mathematical modeling of neuronal

bursting (Bertram 1993 ; Bertram 1994 ; Bertram, et al. 1995 ), electrical coupling of single neurons (Dargaei, et al. 2014 ) and single neuron imaging (Grant, et al. 2001 ; Lee, et al. 2015a ; Lee, et al. 2015b ) and spectroscopy (Grant, et al. 2000 ). Using high field diffusion tensor imaging (DTI), high resolution tractography analysis was used to generate connecting paths or edges between regions of interest within the ABG (Basser, et al. 1994 ; Mori and Zhang 2006 ). These reconstructed edges are principally tracks that follow the changes in neural fiber orientation that can be detected non-invasively through the DTI technique. The DTI-based track network was used to construct entries of the adjacency matrices that correspond to the connections among known labeled vertices. Both binary and weighted analyses were performed on these matrices. Graph properties were derived and compared to lattice and random networks to investigate the small-worldness of the experimental data using the adjacency matrices to represent the graphs of interest.

Although graph theory recently has been applied to networks within the human brain (Wierenga, et al. 2016 ), to our knowledge, this study is the first to apply graph properties to experimental measurements made within neural ganglia. Due to the density and size of the neurons in the aplysia ganglion as well as the acquired resolution, the graph theoretical analysis of DTI tractography for such models may provide the most accurate properties (and potential biomarkers) of structural connectivity in neural networks. This approach provides a foundation to probe the impact of different variables and perturbations to verify the reliability and credibility of such markers.

# CHAPTER 3

# BACKGROUND

Structural connectivity in neural tissues constructs a graph with vertices that correspond to the local communities and edges that are obtained from the DTI-based tractography. Such networks can be interpreted to the corresponding incidence (Fulkerson and Gross 1965 ) and adjacency matrices (Cvetković, et al. 1980 ) to derive the properties of the network. Incidence matrices can be useful in term of tracking labeled connections, but they do not provide the properties of the end points or the path functions. In contrast, adjacency matrices label the vertices and express the existing connections for both binary and weighted graphs. Such matrices are key for vertex properties that can be globalized for the entire network.

The size of the incidence matrix of a graph is $n \times m$ corresponding to connections of $n$ vertices that have been established by $m$ labeled edges. Therefore, it is descriptive of the cardinality and size of the graph (Gutman, et al. 2009 ):

$$IncMatrix(G)_{ij} = \begin{cases} 1 & for\ v_i\ encident\ with\ edge\ j \\ 0 & otherwise; \end{cases}$$

On the other hand, adjacency matrices are concerned only with the existence of an edge that connects two vertices. As such, nodes are labeled without regard to or significant concern for labeling the edges. This approach yields symmetric matrices with a main diagonal of entries of 0, following the assumption that graph vertices do not auto-regulate themselves (Cvetković, et al. 1980 ):

$$AdjMatrix(G)_{ij} = \begin{cases} 1 & for\ v_i\ and\ v_j\ are\ connected \\ 0 & otherwise; \end{cases}$$

These matrices are key in graph theory for extracting properties that can classify network behaviors. Graph properties are a set of parameters that probe the magnitude and velocity of the

communication within a given network. For instance, the clustering coefficient of a graph measures the probability that two neighboring nodes around a specific vertex are connected. The clustering coefficient provides a diagnosing probe that determines key vertices in the graph as well as the network's ability to circulate information in open and closed neighborhoods. For a specific vertex *i* with *e* edges and *k* neighbors, the clustering coefficient $C_i$ takes the form (Watts and Strogatz 1998 ):

$$C_i = \frac{e_i}{\binom{k_i}{2}} . \quad [1]$$

This measurement can be expanded from a single node to provide an averaged total clustering coefficient that reflects the global clustering in the graph (Watts and Strogatz 1998 ):

$$C_G = \frac{1}{N}\sum_{i=1}^{N} C_i . \quad [2]$$

The clustering defined in Eq. 2 is sufficient for graphs that are equipped with binary edges that are equivalent in weight. Most real networks do not exhibit such property. Instead, the circuits in these graphs have preferential paths that are coupled with significant traffic intensity when compared to the rest of the connecting edges. In many cases, such unbalanced communication drives existing edges to vanish when normalized. Various approaches are proposed in order to account for the weight of connections (Barrat, et al. 2004 ; Onnela, et al. 2005 ; Saramäki, et al. 2007 ). In this study, the weighted clustering coefficient is used to evaluate the weighted clustering of individual points in the graph as a function of the vertex edges $k_i$, vertex strength $s_i$, edge intensity: $w_{ij}$ and $w_{ih}$, and the entries of connections $a_{ij}, a_{ih}, and\ a_{jh}$in the corresponding adjacency matrix. The weighted clustering coefficient of the vertex *i* is (Barrat, et al. 2004 ):

$$C_i^w = \frac{1}{s_i(k_i-1)}\sum_{j,h}\frac{(w_{ij}+w_{ih})}{2} a_{ij}a_{ih}a_{jh} . \quad [3]$$

Another parameter used extensively in graph analysis is the characteristic path length of a network (Wasserman and Faust 1994 ). This parameter measures the geodesic distance $L_{ij}$ that connects two generic nodes $i$ and $j$. For a vertex $i$ in a parallel system, there can be as many as $N-1$ short characteristic distances. The average characteristic path length in a graph with $N$ nodes is defined as (Watts and Strogatz 1998 ):

$$L = \frac{\sum_i \sum_j L_{i,j}}{N(N-1)}. \quad [4]$$

If $d_{ij}$ is the shortest characteristic path length that connects a node $i$ by its exhibited distinct adjacent edges, the efficiency $E(G_i)$ of $i$ is defined as the inverse of $d_{ij}$ . So, for a local subgraph with $\tilde{N}$ vertices, the local efficiency $E_{loc}$ takes the form (Latora and Marchiori 2001 ):

$$E_{loc} = \frac{\sum_{i \neq j \in G} E(G_i)}{\tilde{N}}. \quad [5]$$

Similarly, the global efficiency of a network is the sum of the individual efficiencies of each vertex averaged over the number of nodes $N$ in a parallel system in which every vertex contributes to the circulated information through its edges (Latora and Marchiori 2001 ):

$$E(G) = \frac{\sum_{i \neq j \in G} {}^{1}/_{d_{ij}}}{N(N-1)}. \quad [6]$$

The regular lattice network is intolerant to rewiring in the graph and maintains the degree for each vertex in the network, where degree is defined as the number of edges belonging to a specific vertex. As a result, lattice graphs yield the longest average characteristic path length along with a high clustering coefficient. Lattice graphs, therefore, display high local efficiency due to high clustering and low global efficiency due to the relatively large average characteristic path length. On the other hand, random networks obey the highest rewiring probability, therefore, resulting to a significant decrease in the clustering and the averaged geodesic distance

of the graph. Such behavior is coupled with an efficiency that is low in local subgraphs but high on the global scale.

Small-world networks (Watts and Strogatz 1998 ) define a category of graphs that maintain high clustering coefficient by minimizing the rewiring of graph vertices, but achieve a dramatic decrease in the characteristic path lengths from small violations of the order in a regular lattice (Figure1 (Watts and Strogatz 1998 )). As such, relatively high local and global efficiencies are observed simultaneously in graphs that exhibit small-world properties. Small world properties appear at a small rewiring probability ($p$) and, therefore, foster an early increase in the global efficiency because of the path length's high sensitivity to rewiring as compared to the clustering coefficient (Watts and Strogatz 1998 ).

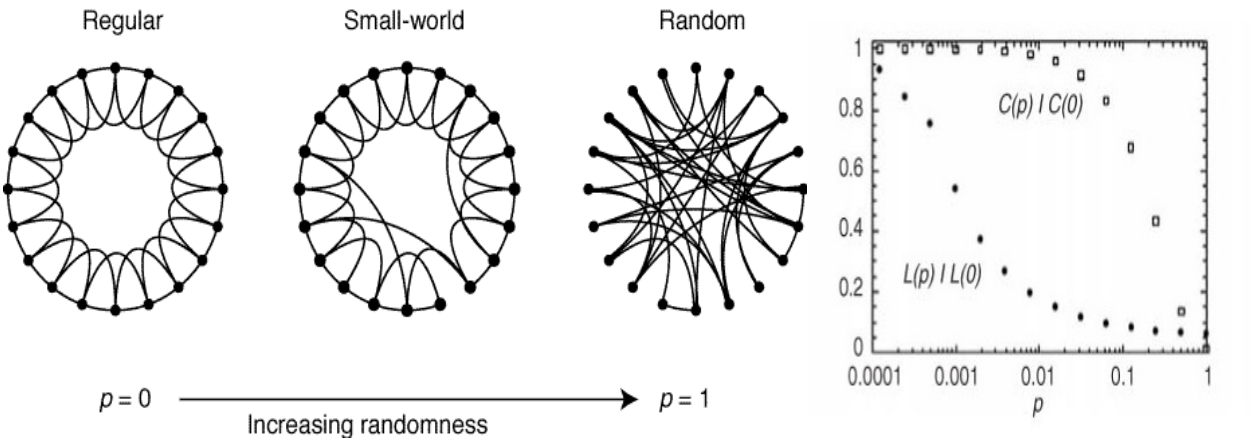


**Figure 1:** In this example, it is demonstrated that as the rewiring probability $p$ increases, the clustering of the small world network $C(p)$ is maintained relatively close to the clustering of the regular lattice $C(0)$. On the other hand, the characteristic path length of the small world network $L(p)$ declines rapidly when compared to the path length of the lattice network $L(0)$. As such, the small world network behavior allows for efficiency that is high locally and globally (Watts and Strogatz 1998 ).

One challenging open question in graph theory is how to identify quantitatively a small-world network. Along with the efficiency measurements defined earlier, other metrics have been suggested to quantify the small-worldness of a network. The small world coefficient $\sigma$ is used to

investigate the graph-clustering ratio with respect to random networks when compared to the path length ratio with respect to lattice network (Humphries and Gurney 2008 ):

$$\sigma = \frac{\gamma}{\lambda}, \quad [7]$$

where $\gamma = {}^{C}/_{C_{random}}$ and $= {}^{L}/_{L_{lattice}}$ . However, fluctuations in the clustering coefficient for random networks along with variations of the path length in lattice graphs as a function of the graph order and size have been challenges for the small world coefficient. As a result, σ is mostly an assessment of randomness in a given network.

The novel small world metric $\omega$ is another suggested measurement to identify a graph that exhibits the proprieties of a small-world network (Telesford, et al. 2011 ):

$$\omega = \frac{L_{random}}{L} - \frac{C}{C_{Lattice}}. \quad [8]$$

Despite its limitations, including vulnerability to significant changes in network order and graphs with particular hub distributions, $\omega$ is capable of locating a network on the continuum from lattice to random networks. This feature appeals to the aim of using graph theoretical analysis to provide biomarkers and reference data for structural connectivity in neural ganglia.

Once the size and fractional probability of connections in a small world network are determined, mathematical simulating tools such as the Watts-Strogatz (WS) model can be used to simulate enlarged networks based on measured graph properties, such as the degree and rewiring probability. The rewiring probability is determined by comparing the graph of interest to a regular lattice network with same number of connections. The fractional probabilities of the violating trails yield the tolerated rewiring. Increasing the order of the network challenges the robustness of the measured graph with respect to its small world classification while evaluating key graph properties such as clustering and path length with a higher number of vertices.

# CHAPTER 4

# MATERIALS AND METHODS

## 4.1 Animal Model

Several aplysia were kept in an aquarium filled with artificial seawater (ASW) until time of excision. For each sample, one aplysia was gently removed from the aquarium and placed into a dissection tray. 10 mL of anesthesia (379 mM $MgCl_2$ and 15 mM HEPES) were injected to three points along the edge of the foot; the head, middle, and tail. The slug was allowed to lie until completely relaxed at which point a scalpel was used to cut along the edge of the foot, being careful not to cut deeper than necessary. The skin was then pulled back and pinned, exposing the organs. The ink sac and stomach were gently pushed aside to reveal the abdominal ganglion. A probe was used to lift the ganglion away from the body wall and surgical scissors were used to snip the brachial nerves about 3-5 mm from the ganglion, freeing it from the body. After gross dissection of nerves and connective tissue, the ganglion was fixed for 24 h in 4% paraformaldehyde. The remaining ganglia (cerebral, pedal and buccal) also were isolated, and the remains properly discarded.

The following day, the fixed ganglion was washed three times in fresh ASW over 24 h. Then the ganglion was freed of any remaining external fibrous tissue and placed into a small glass NMR capillary (2.5-mm OD) filled with ASW for scanning. Each ganglion was positioned such that the brachial nerves extended orthogonal to the tube's surface. The tube was sealed on either end with wax to prevent leakage of ASW from the sample.

### 4.2 DTI Acquisition

Diffusion data were acquired for twelve separate samples (*N=12*) at 11.75 T using Paravision and the 500-MHz magnet located at the FAMU-FSU College of Engineering. Before each run, a shim was performed to maximize homogeneity of the magnetic field, followed by setup scans to assess linewidth and calibrate the RF transmit power and receiver gain. After localizing images, DTI data was collected over a total acquisition time of 19.5 h using a multi-slice, diffusion-weighted 2D spin echo sequence. The acquisition parameters consisted of $\Delta$=21 ms, $\delta$=3 ms, matrix=100×100, TE = 30 ms, TR = 2 s, FOV = 5x5 mm, and slice thickness = 150 μm. An acquisition resolution of 50x50x150 μm was achieved (Figure 2a&b). A total of 22 pulsed field experiments were used to encode diffusion, with four unweighted data acquisitions equally dispersed among directionally unique and optimally arranged samplings of 18 diffusion weighted acquisitions whose pulsed field gradient orientation was described by the electrostatic dispersion on the surface of a unit sphere (Jones and Leemans 2011 ).

The resulting images then were converted to DICOM format and processed with DSI Studio (Yeh, et al. 2013a ) to obtain the full anisotropic diffusion characterization of the neural tissue. Based on the processed DTI data, a 4x4 selection of equally-sized and equidistant regions of interest (ROI) was chosen for each sample such that all lay within the body of the ganglion (Figure 2c). The fractional anisotropy (FA) and apparent diffusion coefficient (ADC) were calculated for each ROI as the mean for all contained voxels. These 16 ROIs constitute the nodes used for network analysis and evaluation by graph theory.

### 4.3 Graph Theoretical Analysis

For tractography analysis, the 16 ROI-based nodes in each ganglion were used to establish a track network with the following cutoffs and thresholds: *Track Counts* $=10^6$, *FA threshold* $= 0.2$ and *Angular Threshold* $= 30°$. These values were defined empirically based on the criteria of establishing local communities that excluded isotropic water and achieved a parallel system in which each node displayed at least one connection to another node (Latora and Marchiori 2001 ). The tracks thusly generated constitute the edges of the network analysis. The graph properties of experimental data were extracted using MATLAB R2015b (Mathworks, Natick, MA) to obtain the clustering coefficients, local and global efficiency, and the characteristic path lengths of the binary adjacency matrices corresponding to unweighted, undirected graphs (Bounova and de Weck 2012 ; de Reus, et al. 2014 ). These properties were averaged for the structural networks of $N=12$ ganglia using the same geometry and threshold parameters to determine if a default structural network was evident. In addition, the small-world properties (Watts and Strogatz 1998 ), namely high clustering as seen in lattice networks and a relatively small rewiring probability that dramatically decreases average characteristic path length for enlarged networks, were evaluated for each network.

Experimental results and networks were compared to two Watts-Strogatz (WS) networks that were generated to include 16 local communities while maintaining the same average degree as the experimental data. These WS networks were assigned rewiring probabilities of 0 and 1 corresponding to lattice and random networks, respectively. The properties of these simulated networks were derived from their corresponding adjacency matrices using the same algorithms as those for quantifying experimental data. The node degree distribution of the experimental data was compared to the WS lattice model having the same cardinality to confirm the deviation of

experimental data. Finally, a graph of 512 nodes was simulated for the same rewiring probability and degree as the experimental structural networks for comparison to a regular lattice and random network of the same order (512 nodes) and average degree (mean degree of ABG nodes ~ 4). For all data, the novel small-world metric (ω) (Telesford, et al. 2011 ) was used along with small world coefficient (σ) (Humphries and Gurney 2008 ) as quantitative probes to verify the small-world properties of the abdominal ganglion experimental networks in comparison to WS lattice and random simulated graphs of equivalent degree and order.

In order to assess the intensity of the traffic through individual vertices in experimental data, the weighted clustering coefficient (Barrat, et al. 2004 ) for each node was measured. Descriptive weighted matrices were generated from DTI-tractography data for every sample to describe the quantity of the edges that connect a node to another. For this purpose, the same labeling of the nodes defined in the binary analysis was employed. The weighted graph analysis was performed only for the clustering assessment to compare it with the obtained clustering coefficients for the corresponding unweighted graphs. The centrality of the selected local communities was investigated to define the most connected hubs in the selected ROIs. The magnitude of the centrality of these vertices is compared to the corresponding weighted clustering coefficients to determine the fate of information traveling through these hub points in the neural tissue. Finally, the graph properties reconstructed by the connectivity between nodes were assessed against the mean FA and ADC measurements for the ROIs as a function of the immediate geometrical node neighbors.

### 4.4 Statistics

Statistical Package for the Social Sciences (SPSS) version 20.0 (Armonk, NY:IBM Corp, 2011) was used for statistical analysis. One-way ANOVA method is used for mean comparison along with Tukey's post hoc test.

### 4.5 Histology

Isolated ganglia were dissected using the above procedure. These ganglia were immersion fixed in 4% paraformaldehyde as previously described. Using standard histological methods, these fixed ganglion were imbedded in paraffin and sectioned at 15 μm thickness. These slices were mounted individually on slices and treated to remove the effects of fixation. Using conventional immunohistochemical techniques, the ganglia were with DAPI to identify nuclear regions and FITC to localize cytoplasmic regimes.

The ganglia were imaged using a fluorescent microscope (MODEL, VENDOR) with appropriate filters to acquire separate channels of DAPI (blue) and FITC (green) data. Images from these channels were processed and overlaid using Photoshop (Adobe, CITY) to provide anatomical references for the distribution of major neurons within the ganglion.

# CHAPTER 5

# RESULTS

DTI images were reconstructed and fractional FA and ADC maps were generated using DSI studio (Jiang, et al. 2006 ; Yeh, et al. 2013b ) (Figure 2a & b). FA and ADC values were measured for the body of the ABG and the branchial nerves (Table 1). Significant difference in FA measurements was found between the ganglion body and the branchial nerves (Figure 3). For graph theoretical analysis, 16 regions of interests (ROIs) were assigned consistently for each ABG (*N=12*) and DTI based tractography (Figure 2c) with specific tracking parameters was used to establish the connecting edges and their corresponding weights within the network (Figure 2d & e) (Bastian, et al. 2009 ). The graph properties based on the analysis of 16 nodes across the samples are displayed in Table 1.

Experimental results and networks were compared to two Watts-Strogatz (WS) networks that were generated to include 16 local communities while maintaining the same average degree as the experimental data. These WS networks were assigned rewiring probabilities of 0 and 1 corresponding to lattice and random networks, respectively. Additionally, a graph of 512 nodes was simulated for the same rewiring probability and degree as the experimental structural networks for comparison to a regular lattice and random network of the same order (512 nodes) and average degree (mean degree of ABG nodes ~ 4).

With relatively high clustering of 0.17 ± 0.05 (Table 1) when compared to the mean clustering of 0.09 for random graphs (averaged over 100 generated random networks) equivalent in size and order, the experimental data exhibited small world properties (Figure 4) that were verified quantitatively by the small worldness coefficient(Humphries and Gurney 2008 ) and the novel small world metric (Telesford, et al. 2011 ). Notably, the experimental data yields $\sigma$ and $\omega$

values that fall between the extremes of the random and lattice networks. According to the work by Humphries and Gurney (Humphries and Gurney 2008 ), the experimental σ greater than 1 lies within the defined range of the small world networks. Likewise, for a small order and using the novel small world metric, the limits developed by Telesford *et al.* 2011(Telesford, et al. 2011 ) would prescribe boundaries for ω of -0.17 (lattice) and +0.69 (random) for 16 vertices, with the experimental ω = +0.16 within these limits and supporting the small world network assumption. Comparing experimental graphs to the WS models equivalent in size and order, experimental data interestingly displays similar characteristic path length of the WS lattice graph (L= 2.40) despite a lower total clustering coefficient, potentially due to the significant node reduction and resultant restrictions of the simulated data. However, another explanation may be the high node centrality of the experimental networks, for which specific local communities (in weight and neighbors) dominate when compared to the rest of nodes.

Using the WS models, a larger nodal network (512) simulated with the same rewiring probability (~0.19) and mean degree (~4) as the experimental data yields the graph properties of Figure 5 and 6, with the lattice and random values for 512 vertices provided for comparison. The analysis shows the stability in transitivity and efficiency of the networks generated from ABG experimental data. The rewiring probability of the simulated data was attained by comparing a regular lattice graph of the same order and number of edges as the ABG networks. The next step was to count the probabilities of violating edges of the lattice order that exist in the acquired networks. These violating paths are, in fact, what yield the exhibited small-word network properties.

The efficiency of these simulated graphs was high locally when compared to the WS random network and high globally when compared to the WS lattice network simultaneously,

which indicates an impressive balance between the transfer of information on both local and universal scales (Figure 6). These properties meet the definition of the small-world networks described by Watts and Strogatz (Watts and Strogatz 1998 ).

To provide insight into the variations of node degree within the same graph, degree distribution analysis that compares experimental networks to equivalent (in average degree and order) lattice network was performed. Experimental data displayed a maximum fractional probability $P(k)$ at degree k = 4 that corresponds to the regular lattice distribution (Figure 7a). However, this distribution was coupled with large variation of the degree among individual vertices. Following node 3, the degree distribution follows the power law behavior indicating that the ABG graphs contain super hub points with an average degree that significantly exceeds the mean degree of the rest of the nodes near the distribution tail (Figure 7b). These hub points likely introduce violating edges that permit the experimental networks to exhibit small world properties.

The individual vertices in experimental data were investigated using a weighted clustering coefficient, centrality, FA and ADC mapping. Findings demonstrate that the properties of these nodes (from graph theory) are not a function of the FA or ADC measurements (Figure 8b &c). For the 16 selected regions, as expected, the centrality was higher in nodes that exhibit higher degrees (Figure 8e). However, the circulated information through these central hubs do not seem to be crucial for maintaining a parallel system due the relatively low weighted clustering coefficients that correspond to these end points. Surprisingly, the weighted clustering coefficient tends to be higher in the areas that have lower centrality (Figure 8f). One explanation of this result is the increasing density of neurons in these specific regions (Figure 8d).

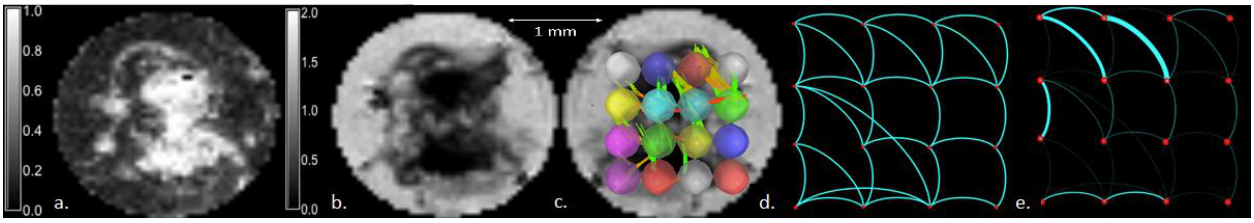


**Figure 2: (a)** FA map generated using DSI studio of an example aplysia ganglion calculated from 18 directionally unique DWI and 4 unweighted MRI. **(b)** Mean ADC map **(c)** 16 local communities were used to assess DTI-based connections between nodes. Tracts were established using thresholds of: FA=0.2, Track Counts=$10^6$ & Angular Threshold=30°. **(d)** Reconstruction of the binary inner-connections using Gephi **(e)** Weighted connecting edges in the neural ganglia

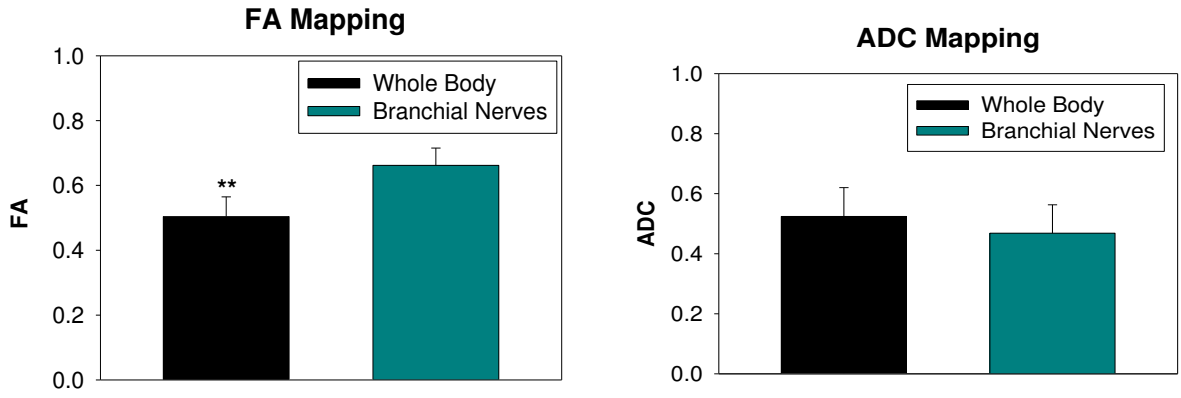


**Figure 3:** FA and ADC measurements to compare the values that correspond to the whole body of the abdominal ganglion versus the values displayed by the branchial nerves.

**Table 1:** Five key graph properties of *N=12* ABG samples were extracted to demonstrate a potential default structural network within the neural tissue. Values are tabulated as means ± standard deviation.

| | Graph Properties (mean ± SD) |
|---|---|
| **Clustering Coefficient** | 0.17 ± 0.05 |
| **Path Length** | 2.38 ± 0.26 |
| **Mean Degree** | 3.56 ± 0.55 |
| **Global Efficiency** | 0.53 ± 0.03 |
| **Local Efficiency** | 0.84 ± 0.02 |

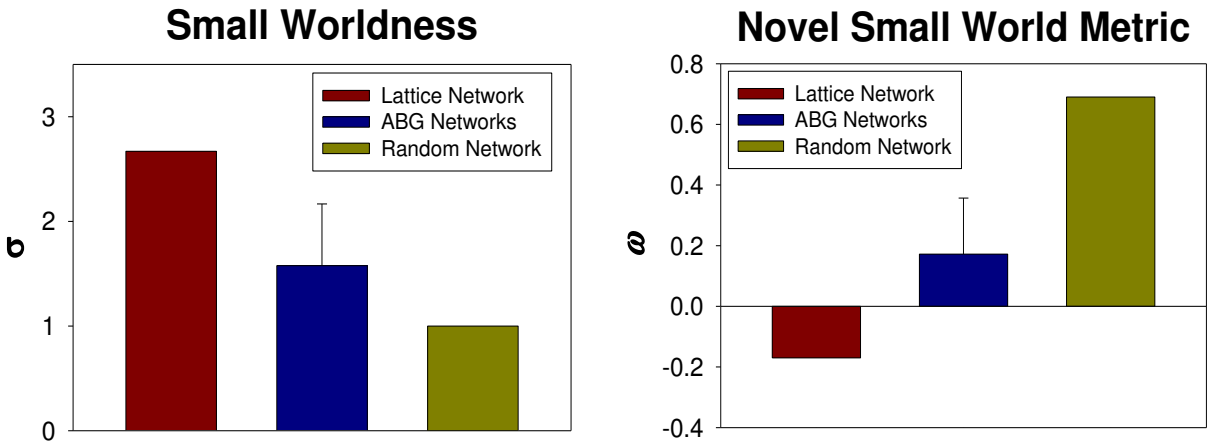


**Figure 4:** Quantitative assessment of the experimental data suggests that the structural network of the ABG exhibits small world properties. The small worldness coefficient recognizes small world network as those with $\sigma > 1$. However, it may include latticized networks in the same category. On the other hand, $\omega$ is capable of locating the network of interest on a continuum from lattice to random properties. The corresponding lattice and random graphs in this analysis carry the same order (16 vertices) and size (mean degree=4) as the ABG networks.

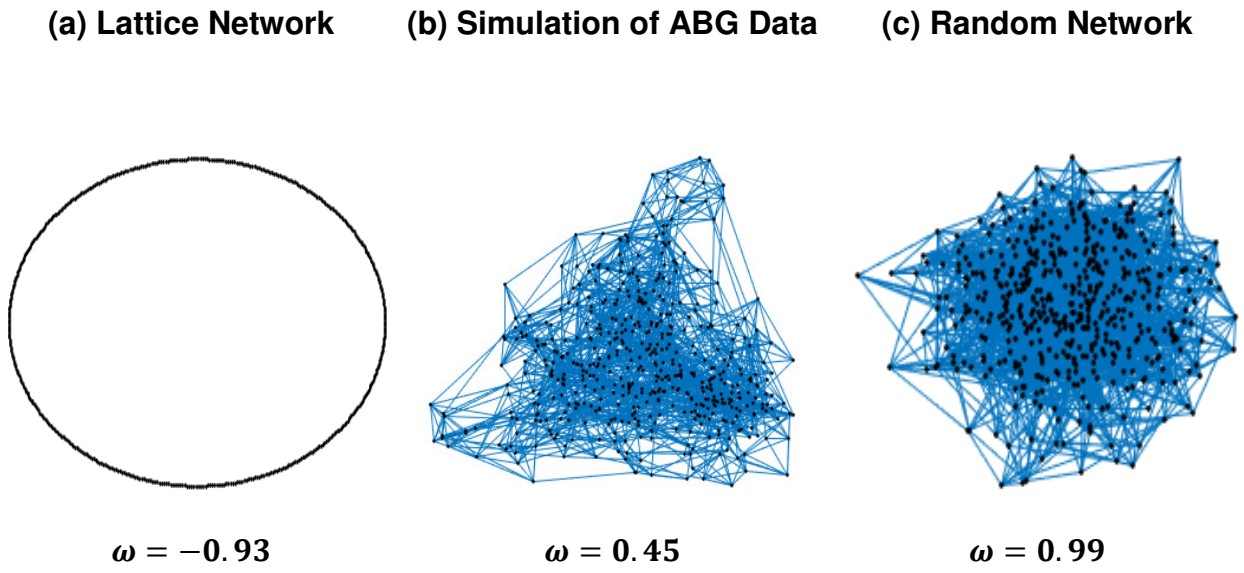


**Figure 5:** Novel small world metric assessment of isomorphic graphs that correspond to mean degree= 4 for: **(a)** lattice network with 512 nodes and rewiring probability $\beta$=0 **(b)** WS Model that carries the rewiring probability of the experimental data $\beta$=0.19 **(c)** Random network with rewiring probability $\beta$=1

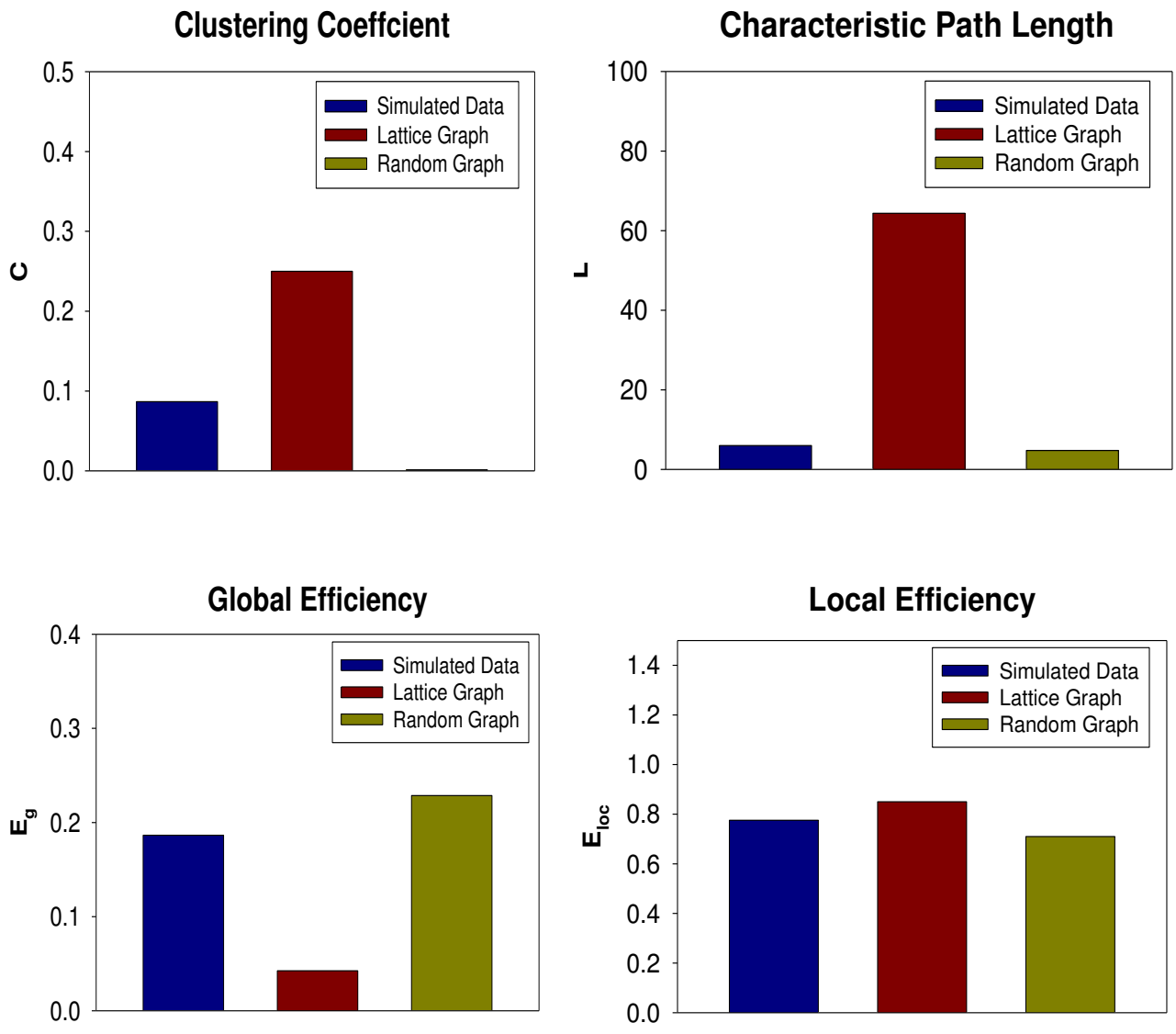


**Figure 6:** Comparison of graph properties of simulated data (with same average degree and rewiring probability as the experimental networks) versus lattice and random graphs with the same order (512 nodes) and size (mean degree of 4).

**(a) Degree Distribution of The Experimental Data vs. Lattice Networks**

**(b) Experimental Data: Scale-Free Property**

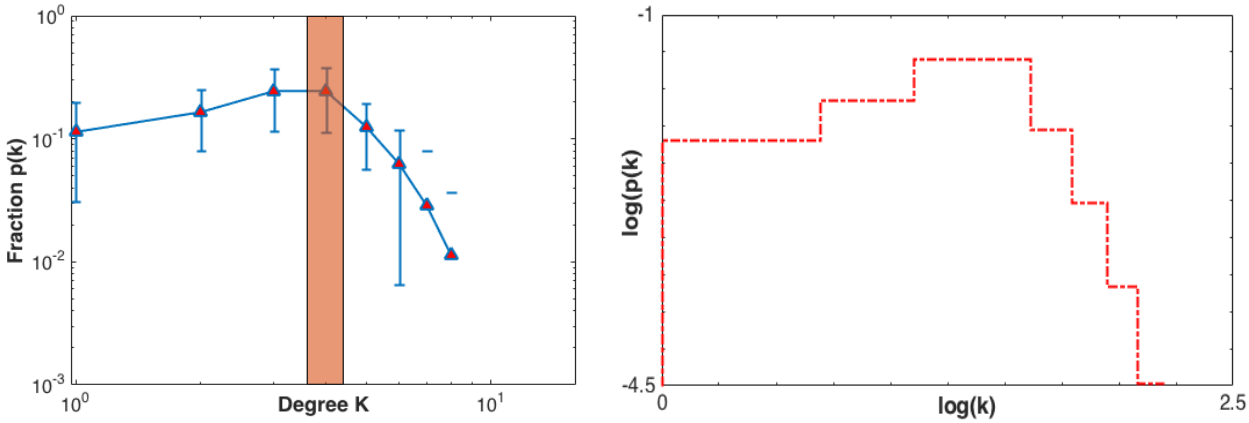


**Figure 7: (a)** Node degree distribution for the experimental data when compared to lattice network that is equivalent in order and mean degree **(b)** Degree distribution follows power law near the tail (k>3) of the distribution. This indicates that existed super hub nodes in the experimental graphs might be the reason for the exhibited small world properties.

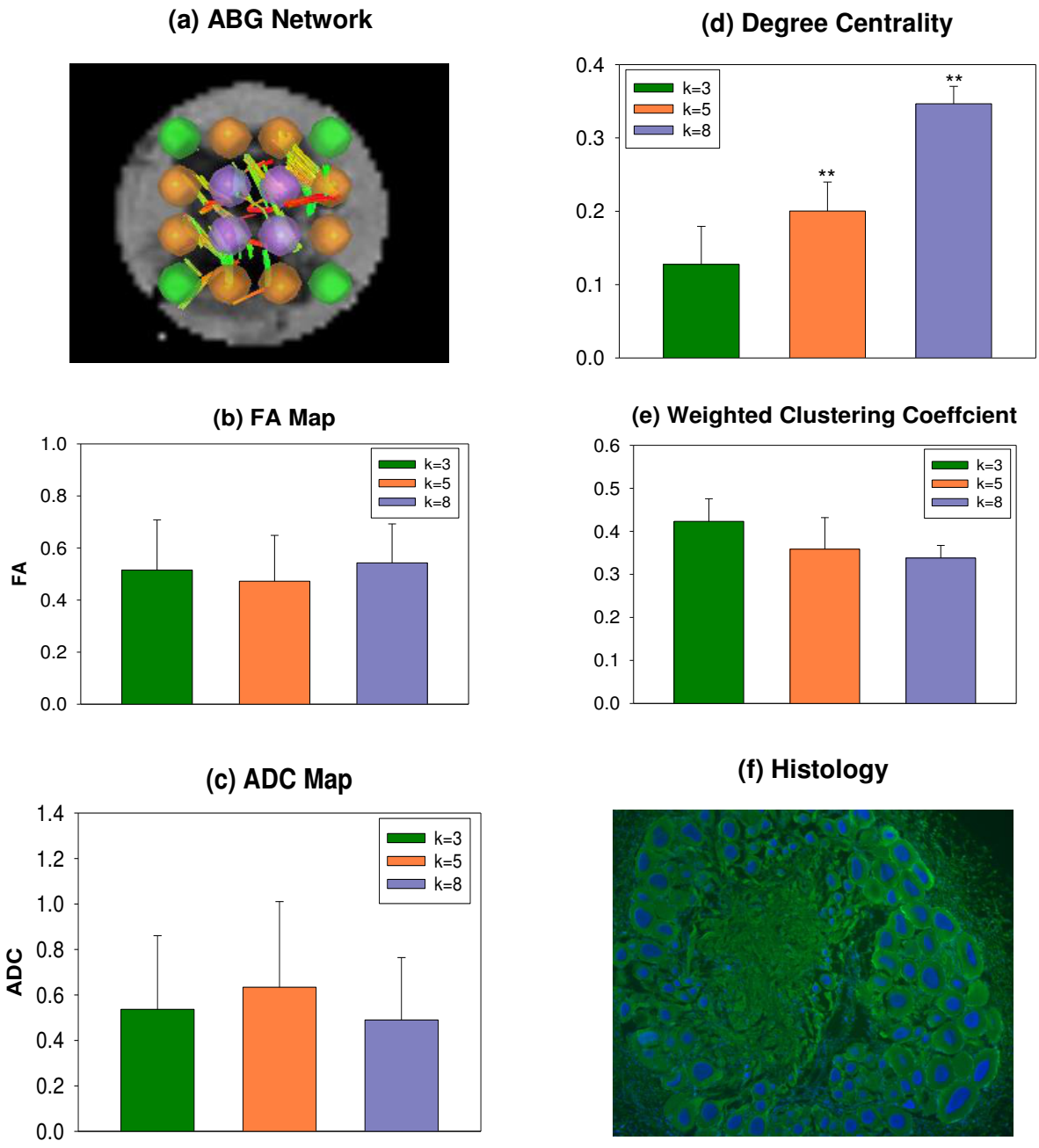


**Figure 8:** Fractional anisotropic map of individual vertices in the experimental networks **(a)** were averaged to investigate correlation between FA **(b)** and ADC **(c)** measurements and the graph properties: centrality **(d)** and weighted clustering **(e)**. The attached histology **(f)** justifies the reduced clustering in central areas when compared to peripheral regions with high neural density. In these graphs, k represents the number of immediate geometrical neighbors.

# CHAPTER 6

# DISCUSSION

This work non-invasively demonstrates for the first time a default structural connectivity within the isolated abdominal ganglia of the *aplysia Californica*. The graph properties of such networks were extracted and found to be relatively consistent among $N = 12$ specimen with low standard deviations for graph properties even given a small number of vertices. The experimental graphs exhibit small world properties when quantitatively evaluated using the small worldness coefficient (Humphries and Gurney 2008 ) and novel small world metric (Telesford, et al. 2011 ). FA and ADC maps were obtained for the isolated abdominal ganglia to investigate the correlations of these measurements with the graph properties of their corresponding nodes. Across vertices as a function of immediate geometric neighbors, there was no significant difference between ROI averaged FA and ADC even though there was significance with respect to the centrality. As a result, the unique graph properties measured are not dependent on volume averaged distributions of DTI parameters outside of the connectivity determined by the much more highly resolved tractography analysis. More critically, the lack of significance between immediate geometric neighbors with respect to the weighted clustering coefficient demonstrates the graph's preference for more critical hubs on the periphery of the ganglion that have a higher number of interconnections within closed clusters even though there exists a lower centrality. This finding is supported by immunohistology, which demonstrates a well-known higher distribution of large neurons in the periphery of the ganglion with more axon density in central regions. The graph theory here applied would suggest that the information circulated among these peripheral hubs is critical for network robustness (Zhang, et al. 2014 ).

Simulated data were generated to probe larger isomorphic networks that carry the same rewiring probability and average degree as the experimental data. Though it is not suggested that WS models are capable of predicting the clustering behavior of specific vertices in neural networks, they can be used to obtain isomorphic graphs for enlarged networks that are assigned with the same properties at the experimental data (Figure 5). It is important to distinguish these simulated unlabeled isomorphic graphs from graphs with vertices that are linked to specific anatomical structures. With that said, isomorphic graphs can aid in visualizing network connectivity as well as determining quantitative properties of networks in an enlarged variable space. The isomorphic graphs of Figure 5 and data of Figure 6 demonstrate the compromise evident in simulated experimental data between the lattice and random extremes with respect to global and local efficiency. Along with the quantitative metrics, this simulated data qualitatively meets the criteria of a small world network and benefits from a small characteristic path length change from the random to achieve significantly higher clustering and local efficiency. The ramifications of this approach to the analysis of neural connectivity suggest that, even on the intraganglion scale, nature establishes a balance of efficiency in the circulation of information that is high locally and globally. Furthermore, the consistency of experimental data with lower nodal sampling and the robust small world properties of experimental and simulated data with higher order suggest the presence of a default structural network for the aplysia abdominal ganglion, which may be present in other neural structures.

For investigating the architecture of the isolated neural ganglia, high resolution DTI is used for the first time to detect the water molecule movements in the neural tissue. The previous literature that studied this neural models did not investigate the structural connectivity nor make use of DTI tractography to probe the communications within neural networks. Integrated with

DTI tractography, the graph theory approach establishes a default structural network for this model that is equipped with robust graph properties that can be detected non-invasively at a subcellular resolution.

Previously, the water diffusion in single *aplysia Californica* neurons was thought to be homogeneous (Hsu, et al. 1997 ). Grant and coauthors (Grant, et al. 2001 ) investigated the exponential decay of the apparent diffusion coefficient in a single isolated neuron using ten diffusion weighted MR images and three directions to conclude that the water diffusion signal in the cytoplasm (Grant, et al. 2001 ) is non-monoexponential and significantly different than the largely monoexponential decay observed in the nucleus (Grant, et al. 2001 ). More recently, the subcellular components of L7 neurons was validated using Magnetic Resonance Microscopy (MRM) and the imaging data were correlated with the well-known histology(Lee, et al. 2015a ).

On the functional side of the neural connectome, the baseline mode of brain function has been reported in the human brain based on the uniformity of the Oxygen Extraction Fraction (OEF) (Raichle, et al. 2001 ). In a related effort, functional MRI (fMRI) was used to demonstrate a default mode network in rat brains that was shared between behavioral, evolutional and physiological features (Lu, et al. 2012 ). At the scale of single neurons, Manganese-Enhanced Magnetic Resonance Imaging (MEMRI) was used by Radecki *et al.* (Radecki, et al. 2014 ) to demonstrate synaptic transmission and functional activity in the buccal ganglion of aplysia by using $Mn^{2+}$ as a $Ca^{2+}$ analog.. They reported detectable variations in neural response that corresponds to a specific sensory stimulus. In comparison, this manuscript investigates the structural component of the connectivity in neural tissue. Although the assessment of functional connectivity advances the state of knowledge about the dynamics of the physiological processes, it is critical to develop techniques and analysis that are capable of investigating (noninvasively)

the default structures that transmit and support such dynamic processes.

Graph theoretical analysis for DTI based tractography recently has become popular for assessing various aspects of connectivity such as asymmetrical human hemispheric networks (Li, et al. 2014 ), reduced characteristic path length and global efficiency in Alzheimer's disease patients(Lo, et al. 2010 ), and the small world network of the cerebral cortex (Sporns and Zwi 2004 ). However, one barrier for verifying the credibility of these markers is a reliance on the accuracy of the attained tracts. The construction of these tracts depends on following the detectable changes of the orientations of the bundles. Hence, if the diameter of these bundles is lower than the acquired resolution, this might result in the reconstruction of misleading tracks. The size and density of the neurons investigated in this study as well as the acquired resolution put the performed graph theoretical analysis at an advantage due to the reduced corresponding errors in DTI-based tractography.

Limitations of this work include the fluctuations of the clustering coefficients that were extracted from random networks as well as the degree distribution. This, in fact, was one of the main reasons for using the novel small world metric that relies on the characteristic path length of random networks. However, other properties such as local and global efficiencies of these networks are somewhat vulnerable and vary greatly when the order of the graph is changed. When evaluating the experimental data, the clustering coefficient tends to be higher for vertices with lower mean degree. Often, as the number of immediate neighbors for a specific node is smaller, the probability for connections to exist within the open neighborhood increases. In fact, this relationship still is one of the challenging barriers for using the clustering coefficient as a stable marker. Though the same parameters for network reconstruction were maintained in each ganglion, DTI-based tractography with different thresholds for the same neural network would

lead to some variations in graph connections as well as the graph properties for such a network.

# CHAPTER 7

# CONCLUSION AND FUTURE WORK

In conclusion, the findings of this study suggest that the quantified graph properties of neural tissue exhibit the features of a small world network with respect to local and global efficiency. Graph theory suggests that the most critical vertices or hubs are not necessarily the most central. This finding is supported by the neuronal distribution, which is generally at the extents of a ganglionic arrangement with the axon density more central. As such, the default structural network suggested by the application of graph theory would appear to represent or at least be sensitive the neuronal distribution and density within the ganglion.

This proposed network behavior has the potential to serve as a significant biomarker of connectivity, even within neural structures. With extension to larger neural networks or even *in vivo* environment, this approach and the potential biomarkers that may be generated by the application of graph theory could be investigated against various variables, including toxicity, electrical activation of neural tissue, aging impacts and osmotic perturbation. As such, this model system and the application of network theory could provide structural and dynamic information about the detection of neural processes and connectivity using non-invasive and non-destructive detection that could be extrapolated to more complex neural tissue and interconnected neural structures.

Future work should focus on evaluating the structural connectivity within the abdominal ganglia using edges that connect individual neurons as the entries for graph theoretical measures. Using such approach allows one to identify dominating neurons and the significance of their connections in order to maintain the robustness of neural networks. Also, using incidence

matrices for the graph theoretical analysis in DTI based tractography will provide a better feedback of the preferred pathways of the axonal bundles. The quantitative properties of the networks examined in this study were solely derived using the adjacency matrix for each graph. As such, only the vertices of these networks were labeled and the connecting edges were only used for establishing connections within the ganglia. When tracking the connecting edges, MR techniques of impedance tomography such as Magnetic Resonance Electrical Impedance Tomography (MREIT) (Oh, et al. 2003 ; Ohin Kwon, et al. 2002 ) or Electrical Properties Tomography (EPT) (Katscher, et al. 2007 ; Voigt, et al. 2011 )can be used to map the conductivity pathways in the neural tissue and, therefore, permits to compare the graph theoretical properties of these connecting edges and the electrical properties that were measured experimentally.

# APPENDIX A

# FA AND ADC MAPPING

**Table 2:** FA and ADC mapping of the body of the ganglion and branchial nerves of aplysia 1:

| Name | Whole Body | Branchial Nerves |
|---|---|---|
| **Voxel Counts** | 5266 | 1074 |
| **Volume (mm^3)** | 1.20529 | 0.245819 |
| **Center x** | 65.6451 | 62.662 |
| **Center y** | 63.7265 | 60.5289 |
| **Center z** | 9.50513 | 10.5801 |
| **Bounding Box x** | 82 | 82 |
| **Bounding Box y** | 81 | 81 |
| **Bounding Box z** | 18 | 19 |
| **Bounding Box x** | 48 | 48 |
| **Bounding Box y** | 44 | 44 |
| **Bounding Box z** | 1 | 2 |
| **FA Mean** | 0.510746 | 0.652877 |
| **FA STD** | 0.26809 | 0.236116 |
| **ADC Mean** | 0.40993 | 0.636988 |
| **ADC STD** | 0.312811 | 0.512065 |
| **Axial Dif. Mean** | 0.579016 | 1.07546 |
| **Axial Dif. STD** | 0.405368 | 0.835869 |
| **Radial Dif. Mean** | 0.325386 | 0.417752 |
| **Radial Dif. STD** | 0.279688 | 0.389313 |

**Table 3:** FA and ADC mapping of the body of the ganglion and branchial nerves of aplysia 2:

| Name | Whole Body | Branchial Nerves |
|---|---|---|
| **Voxel Counts** | 5215 | 842 |
| **Volume (mm^3)** | 1.19362 | 0.192719 |
| **Center x** | 61.5085 | 61.462 |
| **Center y** | 62.3152 | 69.3884 |
| **Center z** | 10.2995 | 13.4537 |
| **Bounding Box x** | 80 | 81 |
| **Bounding Box y** | 79 | 84 |
| **Bounding Box z** | 14 | 16 |
| **Bounding Box x** | 44 | 45 |
| **Bounding Box y** | 46 | 48 |
| **Bounding Box z** | 6 | 11 |
| **FA Mean** | 0.592978 | 0.732601 |
| **FA STD** | 0.257521 | 0.21614 |
| **ADC Mean** | 0.465878 | 0.620643 |
| **ADC STD** | 0.294998 | 0.449637 |
| **Axial Dif. Mean** | 0.74966 | 1.14536 |
| **Axial Dif. STD** | 0.448843 | 0.75147 |
| **Radial Dif. Mean** | 0.323987 | 0.358285 |
| **Radial Dif. STD** | 0.262359 | 0.351545 |

**Table 4:** FA and ADC mapping of the body of the ganglion and branchial nerves of aplysia 3:

| Name | Whole Body | Branchial Nerves |
|---|---|---|
| **Voxel Counts** | 24018 | 1363 |
| **Volume (mm^3)** | 1.37432 | 0.0779915 |
| **Center x** | 127.22 | 125.633 |
| **Center y** | 123.381 | 118.071 |
| **Center z** | 10.1734 | 8.58254 |
| **Bounding Box x** | 178 | 166 |
| **Bounding Box y** | 169 | 167 |
| **Bounding Box z** | 14 | 15 |
| **Bounding Box x** | 81 | 84 |
| **Bounding Box y** | 77 | 85 |
| **Bounding Box z** | 6 | 6 |
| **FA Mean** | 0.435802 | 0.665038 |
| **FA STD** | 0.263813 | 0.232998 |
| **ADC Mean** | 0.468598 | 0.335773 |
| **ADC STD** | 0.294915 | 0.206958 |
| **Axial Dif. Mean** | 0.622619 | 0.575701 |
| **Axial Dif. STD** | 0.34037 | 0.291552 |
| **Radial Dif. Mean** | 0.391585 | 0.215809 |
| **Radial Dif. STD** | 0.281671 | 0.186365 |

**Table 5:** FA and ADC mapping of the body of the ganglion and branchial nerves of aplysia 4:

| Name | Whole Body | Branchial Nerves |
|---|---|---|
| **Voxel Counts** | 5281 | 1022 |
| **Volume (mm^3)** | 1.20872 | 0.233917 |
| **Center x** | 64.6745 | 65.8542 |
| **Center y** | 60.3903 | 63.4031 |
| **Center z** | 9.72373 | 7.27789 |
| **Bounding Box x** | 79 | 79 |
| **Bounding Box y** | 81 | 78 |
| **Bounding Box z** | 15 | 13 |
| **Bounding Box x** | 46 | 46 |
| **Bounding Box y** | 43 | 44 |
| **Bounding Box z** | 2 | 0 |
| **FA Mean** | 0.507689 | 0.781728 |
| **FA STD** | 0.273117 | 0.231284 |
| **ADC Mean** | 0.442509 | 0.332427 |
| **ADC STD** | 0.305483 | 0.390051 |
| **Axial Dif. Mean** | 0.631239 | 0.624093 |
| **Axial Dif. STD** | 0.411696 | 0.685574 |
| **Radial Dif. Mean** | 0.348147 | 0.186594 |
| **Radial Dif. STD** | 0.274908 | 0.280863 |

**Table 6:** FA and ADC mapping of the body of the ganglion and branchial nerves of aplysia 5:

| Name | Whole Body | Branchial Nerves |
|---|---|---|
| **Voxel Counts** | 40271 | 3706 |
| **Volume (mm^3)** | 2.30433 | 0.212059 |
| **Center x** | 120.793 | 128.901 |
| **Center y** | 130.068 | 121.102 |
| **Center z** | 9.32336 | 8.67377 |
| **Bounding Box x** | 172 | 166 |
| **Bounding Box y** | 179 | 172 |
| **Bounding Box z** | 15 | 15 |
| **Bounding Box x** | 68 | 81 |
| **Bounding Box y** | 70 | 71 |
| **Bounding Box z** | 4 | 2 |
| **FA Mean** | 0.474728 | 0.760333 |
| **FA STD** | 0.279714 | 0.240748 |
| **ADC Mean** | 0.624779 | 0.477388 |
| **ADC STD** | 0.387826 | 0.421248 |
| **Axial Dif. Mean** | 0.902474 | 0.909768 |
| **Axial Dif. STD** | 0.533476 | 0.682004 |
| **Radial Dif. Mean** | 0.485927 | 0.261198 |
| **Radial Dif. STD** | 0.363072 | 0.336146 |

**Table 7:** FA and ADC mapping of the body of the ganglion and branchial nerves of aplysia 6:

| Name | Whole Body | Branchial Nerves |
|---|---|---|
| **Voxel Counts** | 72003 | 5762 |
| **Volume (mm^3)** | 4.12004 | 0.329704 |
| **Center x** | 135.745 | 155.427 |
| **Center y** | 130.139 | 126.039 |
| **Center z** | 9.62829 | 9.01493 |
| **Bounding Box x** | 183 | 184 |
| **Bounding Box y** | 179 | 174 |
| **Bounding Box z** | 18 | 20 |
| **Bounding Box x** | 90 | 93 |
| **Bounding Box y** | 72 | 76 |
| **Bounding Box z** | 0 | 0 |
| **FA Mean** | 0.457169 | 0.588844 |
| **FA STD** | 0.258607 | 0.294609 |
| **ADC Mean** | 0.605091 | 0.497813 |
| **ADC STD** | 0.42184 | 0.354689 |
| **Axial Dif. Mean** | 0.833082 | 0.751221 |
| **Axial Dif. STD** | 0.537511 | 0.406955 |
| **Radial Dif. Mean** | 0.491097 | 0.371111 |
| **Radial Dif. STD** | 0.382041 | 0.346725 |

**Table 8:** FA and ADC mapping of the body of the ganglion and branchial nerves of aplysia 7:

| Name | Whole Body | Branchial Nerves |
|---|---|---|
| **Voxel Counts** | 43734 | 5411 |
| **Volume (mm^3)** | 2.50248 | 0.30962 |
| **Center x** | 122.533 | 107.759 |
| **Center y** | 126.092 | 121.802 |
| **Center z** | 9.82693 | 8.57716 |
| **Bounding Box x** | 168 | 151 |
| **Bounding Box y** | 176 | 174 |
| **Bounding Box z** | 17 | 15 |
| **Bounding Box x** | 70 | 71 |
| **Bounding Box y** | 81 | 82 |
| **Bounding Box z** | 2 | 2 |
| **FA Mean** | 0.498054 | 0.618317 |
| **FA STD** | 0.276932 | 0.26889 |
| **ADC Mean** | 0.493994 | 0.45314 |
| **ADC STD** | 0.294005 | 0.306977 |
| **Axial Dif. Mean** | 0.727506 | 0.756639 |
| **Axial Dif. STD** | 0.40998 | 0.475855 |
| **Radial Dif. Mean** | 0.377237 | 0.301391 |
| **Radial Dif. STD** | 0.273842 | 0.263404 |

**Table 9:** FA and ADC mapping of the body of the ganglion and branchial nerves of aplysia 8:

| Name | Whole Body | Branchial Nerves |
|---|---|---|
| **Voxel Counts** | 53400 | 12697 |
| **Volume (mm^3)** | 3.05557 | 0.726528 |
| **Center x** | 124.573 | 120.076 |
| **Center y** | 115.38 | 115.864 |
| **Center z** | 12.5931 | 9.11058 |
| **Bounding Box x** | 182 | 181 |
| **Bounding Box y** | 169 | 155 |
| **Bounding Box z** | 20 | 20 |
| **Bounding Box x** | 74 | 74 |
| **Bounding Box y** | 64 | 67 |
| **Bounding Box z** | 0 | 0 |
| **FA Mean** | 0.578643 | 0.671523 |
| **FA STD** | 0.255968 | 0.270538 |
| **ADC Mean** | 0.365028 | 0.372351 |
| **ADC STD** | 0.275152 | 0.271419 |
| **Axial Dif. Mean** | 0.563571 | 0.631088 |
| **Axial Dif. STD** | 0.401749 | 0.418708 |
| **Radial Dif. Mean** | 0.265755 | 0.242983 |
| **Radial Dif. STD** | 0.234893 | 0.227373 |

**Table 10:** FA and ADC mapping of the body of the ganglion and branchial nerves of aplysia 9:

| Name | Whole Body | Branchial Nerves |
|---|---|---|
| **Voxel Counts** | 34602 | 2770 |
| **Volume (mm^3)** | 1.97994 | 0.158501 |
| **Center x** | 128.944 | 93.8877 |
| **Center y** | 125.891 | 118.347 |
| **Center z** | 10.0379 | 11.8599 |
| **Bounding Box x** | 175 | 168 |
| **Bounding Box y** | 167 | 146 |
| **Bounding Box z** | 19 | 20 |
| **Bounding Box x** | 68 | 67 |
| **Bounding Box y** | 90 | 97 |
| **Bounding Box z** | 1 | 2 |
| **FA Mean** | 0.528049 | 0.684057 |
| **FA STD** | 0.240491 | 0.237878 |
| **ADC Mean** | 0.44957 | 0.513399 |
| **ADC STD** | 0.293326 | 0.314706 |
| **Axial Dif. Mean** | 0.678012 | 0.931273 |
| **Axial Dif. STD** | 0.428845 | 0.511777 |
| **Radial Dif. Mean** | 0.335348 | 0.30446 |
| **Radial Dif. STD** | 0.252016 | 0.269868 |

**Table 11:** FA and ADC mapping of the body of the ganglion and branchial nerves of aplysia 10:

| Name | Whole Body | Branchial Nerves |
|---|---|---|
| **Voxel Counts** | 26776 | 1646 |
| **Volume (mm^3)** | 1.53214 | 0.0941849 |
| **Center x** | 115.332 | 105.101 |
| **Center y** | 128.863 | 122.159 |
| **Center z** | 10.4524 | 12.7345 |
| **Bounding Box x** | 162 | 156 |
| **Bounding Box y** | 169 | 168 |
| **Bounding Box z** | 16 | 17 |
| **Bounding Box x** | 62 | 64 |
| **Bounding Box y** | 74 | 82 |
| **Bounding Box z** | 4 | 5 |
| **FA Mean** | 0.414001 | 0.672889 |
| **FA STD** | 0.258121 | 0.232287 |
| **ADC Mean** | 0.504963 | 0.555101 |
| **ADC STD** | 0.306756 | 0.300641 |
| **Axial Dif. Mean** | 0.677721 | 0.989294 |
| **Axial Dif. STD** | 0.375897 | 0.492174 |
| **Radial Dif. Mean** | 0.418586 | 0.338004 |
| **Radial Dif. STD** | 0.289299 | 0.260754 |

**Table 12:** FA and ADC mapping of the body of the ganglion and branchial nerves of aplysia 11:

| Name | Whole Body | Branchial Nerves |
|---|---|---|
| **Voxel Counts** | 7767 | 674 |
| **Volume (mm^3)** | 1.77773 | 0.154266 |
| **Center x** | 57.6989 | 62.4881 |
| **Center y** | 69.293 | 73.6958 |
| **Center z** | 10.6865 | 7.25371 |
| **Bounding Box x** | 81 | 81 |
| **Bounding Box y** | 93 | 93 |
| **Bounding Box z** | 18 | 19 |
| **Bounding Box x** | 40 | 37 |
| **Bounding Box y** | 44 | 45 |
| **Bounding Box z** | 1 | 1 |
| **FA Mean** | 0.531884 | 0.640389 |
| **FA STD** | 0.16965 | 0.206667 |
| **ADC Mean** | 0.698214 | 0.632764 |
| **ADC STD** | 0.259095 | 0.304218 |
| **Axial Dif. Mean** | 1.09092 | 1.10373 |
| **Axial Dif. STD** | 0.411012 | 0.510724 |
| **Radial Dif. Mean** | 0.501863 | 0.397283 |
| **Radial Dif. STD** | 0.226077 | 0.262417 |

**Table 13:** FA and ADC mapping of the body of the ganglion and branchial nerves of aplysia 12:

| Name | Whole Body | Branchial Nerves |
|---|---|---|
| **Voxel Counts** | 31224 | 2061 |
| **Volume (mm^3)** | 1.78665 | 0.117931 |
| **Center x** | 122.003 | 116.872 |
| **Center y** | 128.607 | 129.492 |
| **Center z** | 9.4787 | 10.9219 |
| **Bounding Box x** | 174 | 172 |
| **Bounding Box y** | 163 | 136 |
| **Bounding Box z** | 18 | 17 |
| **Bounding Box x** | 62 | 65 |
| **Bounding Box y** | 93 | 123 |
| **Bounding Box z** | 2 | 3 |
| **FA Mean** | 0.515011 | 0.597973 |
| **FA STD** | 0.274139 | 0.310464 |
| **ADC Mean** | 0.494046 | 0.345497 |
| **ADC STD** | 0.335974 | 0.310405 |
| **Axial Dif. Mean** | 0.721199 | 0.568049 |
| **Axial Dif. STD** | 0.450838 | 0.486574 |
| **Radial Dif. Mean** | 0.380471 | 0.23422 |
| **Radial Dif. STD** | 0.309973 | 0.265914 |

**Table 14:** FA and ADC mapping across the 12 samples:

| | Fractional Anisotropy | | Apparent Diffusion Coefficient | |
|---|---|---|---|---|
| | **Whole Body** | **B. Nerves** | **Whole Body** | **B. Nerves** |
| 1 | 0.51 | 0.65 | 0.40 | 0.63 |
| 2 | 0.59 | 0.73 | 0.53 | 0.50 |
| 3 | 0.43 | 0.66 | 0.46 | 0.33 |
| 4 | 0.50 | 0.78 | 0.44 | 0.33 |
| 5 | 0.47 | 0.76 | 0.62 | 0.47 |
| 6 | 0.45 | 0.58 | 0.60 | 0.49 |
| 7 | 0.49 | 0.61 | 0.49 | 0.45 |
| 8 | 0.57 | 0.67 | 0.36 | 0.37 |
| 9 | 0.52 | 0.68 | 0.44 | 0.51 |
| 10 | 0.41 | 0.67 | 0.50 | 0.55 |
| 11 | 0.53 | 0.64 | 0.69 | 0.63 |
| 12 | 0.51 | 0.59 | 0.49 | 0.34 |
| Mean | **0.50** | **0.67** | **0.50** | **0.47** |
| Standard Deviation | **0.05** | **0.06** | **0.09** | **0.10** |

# APPENDIX B

# COPYRIGHT PERMISSION LETTER FOR FIGURE 1

**NATURE PUBLISHING GROUP LICENSE**
**TERMS AND CONDITIONS**

Feb 15, 2016

This is a License Agreement between Abdol Aziz O Ould Ismail ("You") and Nature Publishing Group ("Nature Publishing Group") provided by Copyright Clearance Center ("CCC"). The license consists of your order details, the terms and conditions provided by Nature Publishing Group, and the payment terms and conditions.

**All payments must be made in full to CCC. For payment instructions, please see information listed at the bottom of this form.**

| | |
|---|---|
| License Number | 3810320844062 |
| License date | Feb 15, 2016 |
| Licensed content publisher | Nature Publishing Group |
| Licensed content publication | Nature |
| Licensed content title | Collective dynamics of 'small-world' networks |
| Licensed content author | Duncan J. Watts, Steven H. Strogatz |
| Licensed content date | Jun 4, 1998 |
| Volume number | 393 |
| Issue number | 6684 |
| Type of Use | reuse in a dissertation / thesis |
| Requestor type | academic/educational |
| Format | print and electronic |
| Portion | figures/tables/illustrations |
| Number of figures/tables/illustrations | 1 |
| Figures | Figure 1 |
| Author of this NPG article | no |
| Your reference number | 47 |
| Title of your thesis / dissertation | DTI-based connectivity in isolated neural ganglia: A default structural graph in a small world framework |
| Expected completion date | Apr 2016 |
| Estimated size (number of pages) | 60 |
| Total | 0.00 USD |
| Terms and Conditions | |

# REFERENCES


Akhmedov K, Rizzo V, Kadakkuzha BM, Carter CJ, Magoski NS, Capo TR, Puthanveettil SV. 2013. Decreased response to acetylcholine during aging of aplysia neuron R15.

Barrat A, Barthelemy M, Pastor-Satorras R, Vespignani A. 2004. The architecture of complex weighted networks. Proc Natl Acad Sci U S A 101:3747-3752.

Basser PJ, Mattiello J, LeBihan D. 1994. MR diffusion tensor spectroscopy and imaging. Biophys J 66:259-267.

Bastian M, Heymann S, Jacomy M. 2009. Gephi: an open source software for exploring and manipulating networks. ICWSM 8:361-362.

Bertram R. 1994. Reduced-system analysis of the effects of serotonin on a molluscan burster neuron. Biol Cybern 70:359-368.

Bertram R. 1993. A computational study of the effects of serotonin on a molluscan burster neuron. Biol Cybern 69:257-267.

Bertram R, Butte MJ, Kiemel T, Sherman A. 1995. Topological and phenomenological classification of bursting oscillations. Bull Math Biol 57:413-439.

Birner-Gruenberger R, Darnhofer B, Chen W, Monje FJ, Lubec G. 2012. Proteomic characterization of the abdominal ganglion of Aplysia californica—A protein resource for neuroscience. Proteomics 12:2482-2486.

Bounova G, de Weck O. 2012. Overview of metrics and their correlation patterns for multiple-metric topology analysis on heterogeneous graph ensembles. Physical Review E 85:016117.

Bullmore E, Sporns O. 2009. Complex brain networks: graph theoretical analysis of structural and functional systems. Nature Reviews Neuroscience 10:186-198.

Cvetković DM, Doob M, Sachs H. 1980. Spectra of graphs: theory and application. Academic Pr.

Dargaei Z, Colmers PL, Hodgson HM, Magoski NS. 2014. Electrical coupling between Aplysia bag cell neurons: characterization and role in synchronous firing. J Neurophysiol 112:2680-2696.

de Reus MA, Saenger VM, Kahn RS, van den Heuvel MP. 2014. An edge-centric perspective on the human connectome: link communities in the brain. Philos Trans R Soc Lond B Biol Sci 369:10.1098/rstb.2013.0527.

Frost WN, Kandel ER. 1995. Structure of the network mediating siphon-elicited siphon withdrawal in Aplysia. J Neurophysiol 73:2413-2427.

Fulkerson D, Gross O. 1965. Incidence matrices and interval graphs. Pacific journal of mathematics 15:835-855.

Grant SC, Aiken NR, Plant HD, Gibbs S, Mareci TH, Webb AG, Blackband SJ. 2000. NMR spectroscopy of single neurons. Magnetic resonance in medicine 44:19-22.

Grant S, Buckley D, Gibbs S, Webb A, Blackband S. 2001. MR microscopy of multicomponent diffusion in single neurons. Magnetic Resonance in Medicine 46:1107-1112.

Gutman I, Kiani D, Mirzakhah M, Zhou B. 2009. On incidence energy of a graph. Linear Algebra and its Applications 431:1223-1233.

He Y, Evans A. 2010. Graph theoretical modeling of brain connectivity. Curr Opin Neurol 23:341-350.

Hsu EW, Aiken NR, Blackband SJ. 1997. A study of diffusion isotropy in single neurons by using NMR microscopy. Magnetic resonance in medicine 37:624-627.

Humphries MD, Gurney K. 2008. Network 'small-world-ness': a quantitative method for determining canonical network equivalence. PLoS One 3:e0002051.

Jiang H, van Zijl PC, Kim J, Pearlson GD, Mori S. 2006. DtiStudio: resource program for diffusion tensor computation and fiber bundle tracking. Comput Methods Programs Biomed 81:106-116.

Jing J, Cropper EC, Hurwitz I, Weiss KR. 2004. The construction of movement with behavior-specific and behavior-independent modules. J Neurosci 24:6315-6325.

Jones DK, Leemans A. 2011. Diffusion tensor imaging. Magnetic Resonance Neuroimaging. Springer. p 127-144.

Katscher U, Dorniok T, Findeklee C, Vernickel P. 1774. In vivo determination of electric conductivity and permittivity using" Electric Properties Tomography"(EPT). 15:2007.

Klein M, Kandel ER. 1978. Presynaptic modulation of voltage-dependent Ca2+ current: mechanism for behavioral sensitization in Aplysia californica. Proc Natl Acad Sci U S A 75:3512-3516.

Latora V, Marchiori M. 2001. Efficient behavior of small-world networks. Phys Rev Lett 87:198701.

Lee CH, Flint JJ, Hansen B, Blackband SJ. 2015. Investigation of the subcellular architecture of L7 neurons of Aplysia californica using magnetic resonance microscopy (MRM) at 7.8 microns. Scientific reports 5

Li M, Chen H, Wang J, Liu F, Long Z, Wang Y, Iturria-Medina Y, Zhang J, Yu C, Chen H. 2014. Handedness-and hemisphere-related differences in small-world brain networks: a diffusion tensor imaging tractography study. Brain connectivity 4:145-156.

Lo CY, Wang PN, Chou KH, Wang J, He Y, Lin CP. 2010. Diffusion tensor tractography reveals abnormal topological organization in structural cortical networks in Alzheimer's disease. J Neurosci 30:16876-16885.

Lu H, Zou Q, Gu H, Raichle ME, Stein EA, Yang Y. 2012. Rat brains also have a default mode network. Proc Natl Acad Sci U S A 109:3979-3984.

Mori S, Zhang J. 2006. Principles of diffusion tensor imaging and its applications to basic neuroscience research. Neuron 51:527-539.

Newman ME, Watts DJ, Strogatz SH. 2002. Random graph models of social networks. Proc Natl Acad Sci U S A 99 Suppl 1:2566-2572.

Oh SH, Lee BI, Woo EJ, Lee SY, Cho MH, Kwon O, Seo JK. 2003. Conductivity and current density image reconstruction using harmonic Bz algorithm in magnetic resonance electrical impedance tomography. Phys Med Biol 48:3101.

Ohin Kwon, Eung Je Woo, Jeong-Rock Yoon, Jin Keun Seo. 2002. Magnetic resonance electrical impedance tomography (MREIT): simulation study of J-substitution algorithm. Biomedical Engineering, IEEE Transactions on 49:160-167.

Onnela J, Saramäki J, Kertész J, Kaski K. 2005. Intensity and coherence of motifs in weighted complex networks. Physical Review E 71:065103.

Radecki G, Nargeot R, Jelescu IO, Le Bihan D, Ciobanu L. 2014. Functional magnetic resonance microscopy at single-cell resolution in Aplysia californica. Proc Natl Acad Sci U S A 111:8667-8672.

Raichle ME, MacLeod AM, Snyder AZ, Powers WJ, Gusnard DA, Shulman GL. 2001. A default mode of brain function. Proc Natl Acad Sci U S A 98:676-682.

Roberts FS. 1978. Graph theory and its applications to problems of society. SIAM.

Saramäki J, Kivelä M, Onnela J, Kaski K, Kertesz J. 2007. Generalizations of the clustering coefficient to weighted complex networks. Physical Review E 75:027105.

Sporns O, Zwi JD. 2004. The small world of the cerebral cortex. Neuroinformatics 2:145-162.

Telesford QK, Joyce KE, Hayasaka S, Burdette JH, Laurienti PJ. 2011. The ubiquity of small-world networks. Brain Connectivity 1:367-375.

Urban D, Keitt T. 2001. Landscape connectivity: a graph-theoretic perspective. Ecology 82:1205-1218.

Voigt T, Katscher U, Doessel O. 2011. Quantitative conductivity and permittivity imaging of the human brain using electric properties tomography. Magnetic Resonance in Medicine 66:456-466.

Vorster AP, Krishnan HC, Cirelli C, Lyons LC. 2014. Characterization of sleep in Aplysia californica. Sleep 37:1453-1463.

Wasserman S, Faust K. 1994. Social network analysis: Methods and applications. Cambridge university press.

Watts DJ, Strogatz SH. 1998. Collective dynamics of 'small-world'networks. Nature 393:440-442.

Wierenga LM, van den Heuvel, Martijn P, van Dijk S, Rijks Y, de Reus MA, Durston S. 2016. The development of brain network architecture. Hum Brain Mapp 37:717-729.

Yeh F, Verstynen TD, Wang Y, Fernández-Miranda JC, Tseng WI. 2013. Deterministic diffusion fiber tracking improved by quantitative anisotropy.

Zhang J, Ma Z, Chen G. 2014. Robustness of cluster synchronous patterns in small-world networks with inter-cluster co-competition balance. Chaos: An Interdisciplinary Journal of Nonlinear Science 24:023111.

# BIOGRAPHICAL SKETCH

**EDUCATION:**

**Doctoral Student in Biomedical Engineering** May 2014-Present

- Florida State University Tallahassee, FL
- Current GPA: 3.87/4.0

**Masters in Biomedical Engineering** May 2014- May 2016

- Florida State University Tallahassee, FL
- Current GPA: 3.87/4.0

**Post Baccalaureate Study in Chemical Engineering** January 2013-May 2014

- Florida State University Tallahassee, FL
- GPA: 3.85 /4.0

**First Professional degree in Medicine (Medical Doctor)** August 2010

- University of Aleppo Aleppo, Syria
- GPA: 3.19/4.0 (Evaluated by World Education Services)

**MEDICAL TRAINING:**

**Residency, University of Aleppo Hospital and Kennedy Hospital** September 2009-August 2010 Aleppo, Syria

- Tended to patients in the emergency rooms.
- Developed treatment plans under the supervision of the specialized doctors

**RESEARCH EXPERIENCE:**

**Peripheral Tumors of the Head and Neck Area** February 2010-August 2010

**University of Aleppo** Aleppo, Syria

- Under the supervision of Dr. Majd Ghanamah.

**Graduate Research Assistant at the National High** May 2014-Present

**Magnetic Field Laboratory, FSU** Tallahassee, FL

**WORK EXPERIENCE:**

**Research Assistant at the National High Magnetic** May 2014- Present

**Field Laboratory:** Tallahassee, FL

- Traumatic Brain Injury (TBI) assessment using Diffusion Tensor Imaging (DTI) technique.
- DTI-Based Connectivity in Isolated Neural Ganglia: A Default Structural Graph in a Small-world Framework.

**Teaching Assistant at FAMU-FSU College of Engineering:**

- Thermodynamics (EML 3100) Fall 2014
- Mass and Energy Balance II (ECH 3024) Spring 2015

**Peer Tutor at ACE Learning Studio for Calculus** August 2013-May 2014

- Developing new strategies for students to approach problems. Tallahassee, FL
- Preparing students for exams.

**Volunteer at Student Disabilities Resource Center, FSU** Fall 2013-2014

- Note taker and exam scribe. Tallahassee, FL

**AWARDS:**

- Scholarship of Excellence from Mauritanian Ministry of Education 2004-2010
- Mauritanian Military Health Department Scholarship 2006-2010

**LANGUAGES:**

- Fluent in Arabic, French, and English.